Retrieval of cloud parameters from satellite-based reflectance measurements in the ultraviolet and the oxygen A-band

B. van Diedenhoven,[1] O. P. Hasekamp,[1] and J. Landgraf[1]

[1]   We present a new method for the retrieval of cloud fraction, cloud optical thickness and cloud top pressure from measurements of the Global Ozone Monitoring Experiment (GOME) and Scanning Imaging Absorption Spectrometer for Atmospheric Chartography (SCIAMACHY), relevant for the retrieval of trace gas abundances in cloudy atmospheres. The presented algorithm makes use of the measurements of the oxygen A-band between 758 and 770 nm and additionally of measurements in the ultraviolet between 350 and 390 nm. In addition to the cloud parameters, information about the surface reflection is retrieved. It is shown that measurements in the oxygen A-band alone contain significant information about only two cloud parameters. By adding measurements in the ultraviolet, information about cloud fraction, cloud optical thickness, and cloud top pressure can be retrieved. The cloud retrieval algorithm was applied to GOME data, and the results are compared to cloud parameters retrieved from measurements of the Along Track Scanning Radiometer 2 (ATSR-2). The cloud fractions, cloud optical thickness, and cloud top pressures retrieved by our algorithm and the corresponding ATSR-2 values have a median difference of -0.01, 2.5 and -33 hPa, respectively, with 68% confidence intervals of ±0.11, ±7.5 and ±111 hPa, respectively.

Citation: van Diedenhoven, B., O. P. Hasekamp, and J. Landgraf (2007), Retrieval of cloud parameters from satellite-based reflectance measurements in the ultraviolet and the oxygen A-band, *J. Geophys. Res.*, *112*, D15208, doi:10.1029/2006JD008155.

1.   Introduction

[2]   Satellite measurements of reflected sunlight in the ultraviolet (UV), visible, and infrared are extensively used to monitor atmospheric compounds, such as ozone, nitrogen-dioxide (NO_2), sulphur-dioxide (SO_2), water vapor, and aerosols. For these purposes, the Global Ozone Monitoring Experiment (GOME-1 and GOME-2) [*Burrows et al.*, 1999], the Scanning Imaging Absorption Spectrometer for Atmospheric Chartography (SCIAMACHY) [*Bovensmann et al.*, 1999], and the Ozone Monitoring Instrument (OMI) [*Levelt et al.*, 2006] measure the Earth reflectance in the wavelength ranges 240–800, 240–2380, and 270–500 nm, respectively. The large fields-of-view of GOME (320 × 40 km²), SCIAMACHY (60 × 30 km²), and OMI (13 × 24 km²) imply that, on average, about 98%, 94% and 90% of their measurements, respectively, are contaminated by clouds [*Krijger et al.*, 2007].

[3]   Clouds significantly affect the radiation field in the atmosphere because of their relatively high reflectance and because they partly shield the atmosphere below them. Therefore, it is essential to accurately take the effect of clouds into account in the retrieval of trace gas abundances [*Thompson et al.*, 1993; *Koelemeijer and Stammes*, 1999; *Liu et al.*, 2004; *Wang et al.*, 2006]. Here, the cloud parameters needed are the cloud optical thickness, the cloud top pressure, and the relative amount of clouds in the field of view, i.e., the cloud fraction [*Koelemeijer and Stammes*, 1999].

[4]   For GOME and SCIAMACHY, several algorithms to retrieve one or several of these cloud parameters are available [e.g., *Koelemeijer et al.*, 2001; *Rozanov and Kokhanovsky*, 2004; *Joiner et al.*, 2004; *Grzegorski et al.*, 2006; *Van Roozendael et al.*, 2006]. Many of these algorithms retrieve cloud information from measurements in the oxygen A-band and the continuum around it [*Kuze and Chance*, 1994; *Koelemeijer et al.*, 2001; *Rozanov and Kokhanovsky*, 2004]. These measurements are sensitive to the cloud fraction, cloud optical thickness, and cloud top pressure. Since the amount of oxygen in the atmosphere is well known, cloud information can be retrieved from these measurements. However, different combinations of cloud fraction and optical thickness produce nearly the same measurement at the oxygen A-band. For example, Figure 1 shows that two very distinct combinations of cloud fraction and optical thickness produce similar spectra with differences below 0.6%. Given the fact that the total error in forward model and measurement may be expected to be larger than 0.6% [*van Diedenhoven et al.*, 2005], it is

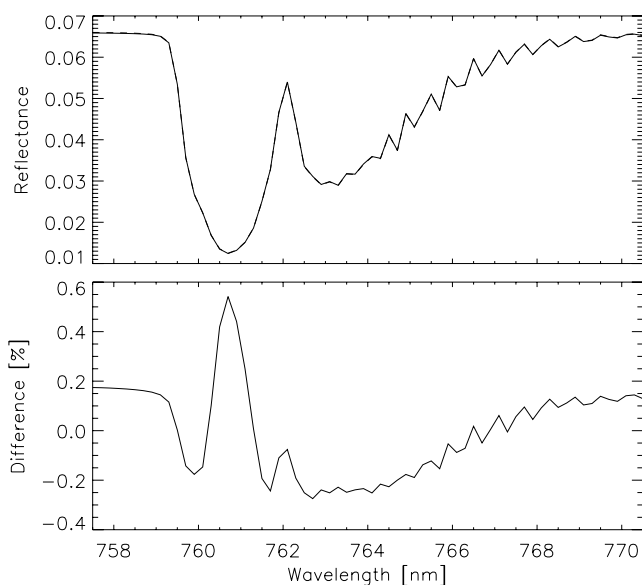[1]SRON Netherlands Institute for Space Research, The Netherlands.

Figure 1. Two forward model calculations in the oxygen A-band (top panel) and their differences (bottom panel). The solid line shows the result of a model calculation assuming a cloud with an optical thickness of 10, a top pressure of 500 hPa, and a cloud fraction of 0.50. The dashed line shows the result of a model calculation assuming a cloud with an optical thickness of 40, a top pressure of 520 hPa and a cloud fraction of 0.30. All calculations are performed for a nadir viewing geometry with a solar zenith angle of 40° and the US standard atmosphere over a black surface. Here the independent pixel approximation [e.g., *Marshak et al.*, 1995] is used.

virtually impossible to retrieve both cloud fraction and optical thickness from oxygen A-band measurements. For this reason, some cloud retrieval algorithms [*Kurosu et al.*, 1999; *Van Roozendael et al.*, 2006] use the higher spatial resolution measurements of the Polarization Measuring Devices (PMDs) to determine the cloud fraction using thresholds for the intensity values defining cloud-free and fully clouded scenes. Subsequently, this value for the cloud fraction is used for the retrieval of cloud top height and cloud optical thickness from oxygen A-band measurements. A drawback of this approach is that the retrieved cloud parameters strongly depend on the chosen threshold values [*Tuinder et al.*, 2004]. Alternatively, a fixed cloud optical thickness can be assumed and so-called effective values of the cloud fraction and cloud top pressure are retrieved [*Kuze and Chance*, 1994; *Koelemeijer et al.*, 2001]. However, the effective cloud parameters may differ significantly from actual cloud parameters. For example, assuming that the actual values of cloud fraction, cloud optical thickness, and cloud top pressure are 0.5, 10, and 500 hPa, respectively, the values of the corresponding effective cloud fraction and effective cloud top pressure are 0.29 and 524 hPa, respectively, when assuming a cloud optical thickness of 40 (see Figure 1). This may cause problems in the retrieval of trace gas amounts. For example, *Wang et al.* [2006] have shown that the use of effective cloud parameters in DOAS based tropospheric NO_2 column retrievals can cause errors >20% in the retrieved column for geometrical cloud fractions larger than 0.5, and errors >10% for geometrical cloud fractions

larger than 0.2. Additionally, effective cloud parameters retrieved from oxygen A-band measurements are generally not representative for other spectral ranges. This is illustrated in Figure 2, which shows two simulated UV reflectance spectra from 350 to 390 nm and their differences, for the same two combinations of cloud parameters as used for the simulations in the oxygen A-band shown in Figure 1. From Figure 2 it follows that the use of effective cloud parameters retrieved from measurements at the oxygen A-band results in errors larger than 3.5% in the spectral range 350–390 nm. This is due to the much stronger contribution of Rayleigh scattered light to measurements in the UV than to measurements at the oxygen A-band. In turn, the large differences between the two spectra in Figure 2 can be explained by the fact that the spectrum calculated for the effective cloud parameters has a too large contribution of Rayleigh scattering, due to the difference between effective cloud fraction and actual cloud fraction. On the one hand, this means that effective cloud parameters retrieved from oxygen A-band measurements introduce significant errors when used in the UV spectral range. On the other hand, it indicates that the combined use of measurements in the UV and at the oxygen A-band allows the retrieval of independent information about the cloud fraction, cloud optical thickness, and cloud top pressure.

[5] In this paper, we present a new method for the independent retrieval of cloud fraction, cloud optical thickness, and cloud top pressure from GOME and SCIA-MACHY measurements which is based on this concept. For this purpose, measurements at the oxygen A-band from 758 to 770 nm and in the UV from 350 to 390 nm are used. An advantage of our approach in comparison to approaches using only the oxygen A-band is that, in addition to the cloud top pressure, information about both the cloud fraction and cloud optical thickness can be retrieved, instead of only an effective cloud fraction. The retrieved cloud parameters are relevant for the retrieval of trace gas abundances in cloudy atmospheres. The paper is constructed as follows: in section 2, the retrieval approach
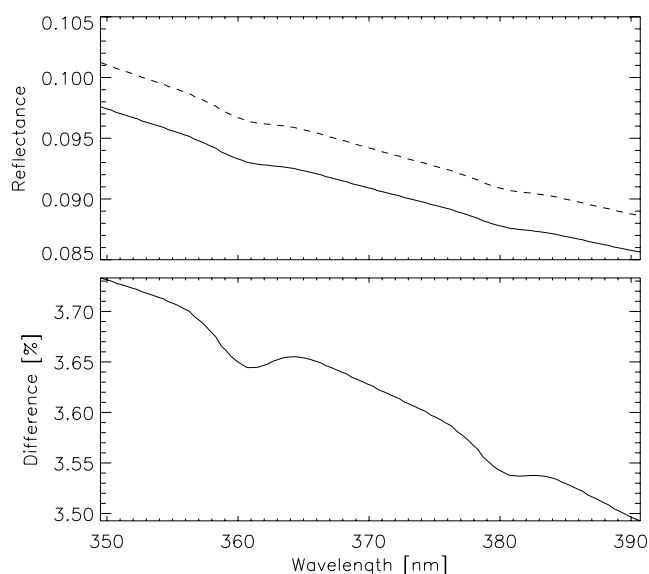

Figure 2. Same as Figure 1 but for the 350- to 390-nm window.

is presented. Section 3 discusses the information content of the measurements, the retrieval noise and regularization errors on the retrieval result, and the sensitivity of the retrieval approach to instrument calibration errors. Also, the relevance of the retrieved cloud parameters to retrieval of tropospheric NO_2 columns is discussed in this section. Next, in section 4, the retrieval concept is applied to GOME measurements, and the results are compared to results of the Fast Retrieval Scheme for Cloud Observables (FRESCO) [*Koelemeijer et al.*, 2001] and cloud parameters retrieved from the Along Track Scanning Radiometer 2 (ATSR-2) instrument. Also, the spectral fitting residuals are discussed in this section. Finally, we conclude the paper in section 5.

2. Retrieval Approach

2.1. Forward Model

[6] Let us define a measurement vector **y**, containing the reflectances measured by GOME or SCIAMACHY in the spectral ranges 350–390 and 758–770 nm. Next, we define an atmospheric state vector **x** that contains the parameters to be retrieved. In our case, these are the cloud fraction, the cloud optical thickness at 550 nm, the cloud top pressure, the surface albedo in both wavelength windows, and their linear spectral dependence. The geometrical thickness of the cloud is assumed to be known a priori. For the retrieval of an atmospheric state vector **x** from the measurement vector **y**, a forward model **F** is needed that describes how **y** and **x** are related, viz.

$$\mathbf{y} = \mathbf{F}(\mathbf{x}) + \mathbf{e}, \qquad (1)$$

with error term **e**. To obtain **F** for a partly cloudy measurement footprint, the independent pixel approximation [e.g., *Marshak et al.*, 1995] is applied, viz.

$$\mathbf{F} = (1 - f_c)\,\mathbf{F}_{\text{clear}} + f_c\,\mathbf{F}_{\text{cloud}}, \qquad (2)$$

where f_c is the cloud fraction and $\mathbf{F}_{\text{clear}}$ and $\mathbf{F}_{\text{cloud}}$ are the components of the forward model for the clear sky and cloudy parts of the measurement footprint, respectively. The main part of the forward models $\mathbf{F}_{\text{clear}}$ and $\mathbf{F}_{\text{cloud}}$ is an atmospheric radiative transfer model. Here, we employ the vector radiative transfer model of *Hasekamp and Landgraf* [2002] and the CODAGS vector radiative transfer model of *van Diedenhoven et al.* [2006] to describe the radiative transfer in the clear sky and cloudy part of the atmosphere, respectively. This provides an efficient forward model for partly cloudy atmospheres. The use of this model allows us to model the polarization-sensitive measurements of GOME and SCIAMACHY [*Hasekamp et al.*, 2002; *van Diedenhoven et al.*, 2005]. In this way, errors due to the polarization correction in the GOME and SCIAMACHY data processing [*Stam et al.*, 2000; *Hasekamp et al.*, 2002; *Schutgens and Stammes*, 2003] are avoided. To simulate the spectral smoothing by the instruments, the instrument response function of *Bednarz* [1995] is used.

[7] For the radiative transfer calculations, the absorption line parameters of the oxygen A-band are taken from the *HITRAN* 2004 spectroscopic database [*Rothman et al.*, 2005], and a Voigt lineshape is assumed. The cross-section sampling and radiative transfer calculations in the oxygen A-band are performed on a 0.005-nm spectral resolution, which we found to be appropriate for a line-by-line simulation in this spectral range. For the calculation of the cross-sections of the weak oxygen dimer (O_2–O_2) absorption lines around 360 and 380 nm, a Lorentz lineshape is used with widths and center wavelengths taken from *Greenblatt et al.* [1990]. The Rayleigh scattering cross-sections and phase function are taken from *Bucholtz* [1995]. The scattering properties of the cloud particles are calculated using Mie theory [*van de Hulst*, 1957; *de Rooij and van der Stap*, 1984]. The size distribution of the cloud particles is assumed to be log normal, with an effective radius of 6 μm and an effective variance of 0.5 (see *Hansen and Travis* [1974] for the definitions). Furthermore, we assume nonabsorbing cloud particles with a refraction index of 1.335. This results in a scattering phase function with an asymmetry parameter of 0.841. The cloud optical thickness τ_λ at a wavelength λ is obtained from the value τ_{550} at 550 nm via

$$\tau_\lambda = \frac{C_\lambda}{C_{550}}\tau_{550}, \qquad (3)$$

where C_λ and C_{550} are the Mie scattering cross-sections at wavelength λ and 550 nm, respectively. The reflection of land surfaces and snow covered surfaces is modeled by a Lambertian albedo. For retrievals above sea surfaces, the surface reflection is characterized by a modeled ocean reflection matrix. For this, the Fresnel reflection on waves is calculated with the method of *Mishchenko and Travis* [1997], assuming the wind-speed-dependent distribution of surface slopes proposed by *Cox and Munk* [1954]. The Lambertian surface albedo, which is a free parameter in the retrieval, is added to the sea surface reflection matrix.

2.2. Inversion

[8] The aim of an inversion is to find a state vector $\hat{\mathbf{x}}$ for which forward model $\mathbf{F}(\hat{\mathbf{x}})$ and measurement **y** are in optimal agreement. Since the forward model is not linear in the unknown parameters, the solution of the inversion problem has to be found iteratively. Here, in each iteration step n, we replace the forward model in (1) by its linear approximation, i.e.

$$\mathbf{F}(\mathbf{x}) \approx \mathbf{F}(\mathbf{x}_n) + \mathbf{K}\,[\mathbf{x} - \mathbf{x}_n], \qquad (4)$$

where $\mathbf{x}_n$ is the state vector for the iteration step under consideration, and **K** is the Jacobian matrix containing the derivatives of the forward model with respect to the elements of $\mathbf{x}_n$. Thus, element K_{ij} of **K** is defined by

$$K_{ij} = \frac{\partial F_i}{\partial x_j}(\mathbf{x}_n). \qquad (5)$$

The derivatives are estimated using finite differencing. The measurement vector **y** considered here does not contain sufficient information to retrieve all seven unknown parameters, and thus the corresponding inverse problem is ill posed. This means that many combinations of the seven parameters fit the measurement almost equally well within the noise. As a result, the least squares solution to our

Table 1. Sensitivity Study Parameters[a]

Parameter	Value
Cloud optical thickness	10
Cloud top pressure	500 hPa
Cloud bottom pressure	700 hPa
Surface albedo O_2 A-band sea	0.01
Surface albedo UV-window sea	0.05
Surface albedo O_2 A-band vegetation	0.3
Surface albedo UV-window vegetation	0.05
Surface albedo O_2 A-band snow	0.9
Surface albedo UV-window snow	0.9
Surface albedo slope O_2 A-band	0
Surface albedo slope UV-window	0

[a]Unless stated otherwise.

inverse problem is overwhelmed by noise. In order to reduce the effect of noise, we employ the Phillips–Tikhonov regularization method [*Phillips*, 1962; *Tikhonov*, 1963] in a similar way as described in detail by *Hasekamp and Landgraf* [2005]. The most important aspects are summarized in Appendix A.

[9] Here, the retrieval result $\hat{x}$ is a combination of information extracted from the measurements and a priori information and is related to the true state vector $\mathbf{x}_{\text{true}}$ and the a priori state vector $\mathbf{x}_a$ via

$$\hat{\mathbf{x}} = \mathbf{A}\mathbf{x}_{\text{true}} + (\mathbf{I} - \mathbf{A})\mathbf{x}_a + \mathbf{e}_x, \qquad (6)$$

where $\mathbf{e}_x$ represents the error in the retrieval result caused by the measurement error. Furthermore, $\mathbf{A}$ is the averaging kernel of the retrieval (see equation (A5) in Appendix A). The covariance matrix $\mathbf{S}$ of the error in $\hat{x}$ is given by

$$\mathbf{S} = \mathbf{S}_x + \mathbf{S}_r. \qquad (7)$$

Here, $\mathbf{S}_x$ is the retrieval noise covariance matrix given by

$$\mathbf{S}_x = \mathbf{D}\,\mathbf{S}_y\,\mathbf{D}^T, \qquad (8)$$

where $\mathbf{D}$ is the contribution matrix (see equation (A3) in Appendix A), and $\mathbf{S}_y$ is the measurement error covariance matrix. Furthermore, $\mathbf{S}_r$ is the regularization error covariance matrix due to an error on $\mathbf{x}_a$ and is given by

$$\mathbf{S}_r = (\mathbf{I} - \mathbf{A})\,\mathbf{S}_a\,(\mathbf{I} - \mathbf{A})^T, \qquad (9)$$

where $\mathbf{S}_a$ is the a priori error covariance matrix.

[10] When the first-guess state vector is far from the true state vector, the linear approximation of (4) hampers the iterative solution of the inverse problem, resulting in no convergence of the fit. To improve the convergence, the Levenberg–Marquardt method [*Levenberg*, 1944; *Marquardt*, 1964] is used. The combination of the Levenberg–Marquardt method and the Phillips–Tikhonov method is summarized in Appendix B. The convergence of the algorithm including the Levenberg–Marquardt method is checked using an ensemble of simulated measurements with randomly distributed cloud parameters. About 90% of the retrievals converged. This is in accordance with the convergence rate of retrievals on real GOME measurements. To improve

on this convergence rate, an unconverged retrieval could be repeated with different first-guess values. This is however not yet implemented in the current version of the retrieval algorithm.

3. Sensitivity Study

[11] In this section, we will investigate the information content of reflectance measurements in the UV from 350 to 390 nm combined with those at the oxygen A-band from 758 to 770 nm for cloud parameter retrievals. The information content will be compared to that of retrievals using only measurements in the oxygen A-band, as commonly used in cloud retrieval algorithms [*Kuze and Chance*, 1994; *Koelemeijer et al.*, 2001; *Rozanov and Kokhanovsky*, 2004]. For the combined oxygen A-band and UV measurements, also the retrieval noise and regularization errors are discussed. Furthermore, we will asses the sensitivity of the cloud parameter retrievals to instrument calibration errors.

[12] For this study, GOME measurements are simulated for the US standard atmosphere using the cloud and surface parameters given in Table 1. A nadir viewing geometry is used with a solar zenith angle of 40°. The wind speed needed to characterize Fresnel reflection on the sea waves is set to 7 m/s. To simulate the measurement noise, a Gaussian noise contribution is added to the simulated measurements. The GOME measurement noise in the UV and oxygen A-band windows is about 0.1%. However, we use a noise contribution of 0.5% to account for forward model and measurement errors with a random-like structure, such as errors due to the "undersampling" effect [*Chance et al.*, 2005; *van Deelen et al.*, 2007] and due to the Ring effect [*Joiner et al.*, 2004; *Landgraf et al.*, 2004] in the UV and errors in spectroscopy data and the instrument response function [*Yang et al.*, 2005; *Tran et al.*, 2006; *van Diedenhoven et al.*, 2005] in the oxygen A-band region. It is important to note that the conclusions made in this section are not significantly different when assuming noise contributions of 0.1–1%.

3.1. Information Content

[13] The information content of a measurement vector can be studied by investigating the sensitivity of the retrieved parameters to a priori information, $\partial\hat{x}_i/\partial x_{a,i}$. As can be concluded from (6), the diagonal terms a_{ii} of $\mathbf{A}$ describe this sensitivity, viz.

$$\frac{\partial\hat{x}_i}{\partial x_{a,i}} = 1 - a_{ii}. \qquad (10)$$

For example, when $\partial\hat{x}_i/\partial x_{a,i} = 0$, the corresponding retrieved parameter is not dependent on its a priori value and thus determined purely from the measurement.

[14] Figure 3 shows $\partial\hat{x}_i/\partial x_{a,i}$ for a measurement vector containing only measurements in the oxygen A-band above sea, vegetation, and snow surfaces. Above sea and vegetation surface types, the oxygen A-band measurements contain significant information about the cloud top pressure and cloud fraction. However, these measurements contain little additional information about the cloud optical thickness. Information about the surface albedo is hardly available for
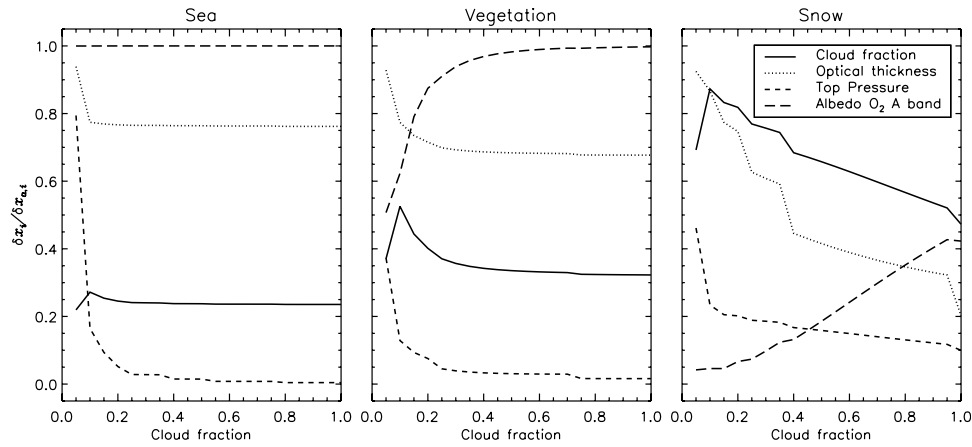
Figure 3. Derivatives of retrieved cloud and surface parameters with respect to their a priori values as a function of cloud fraction, for a measurement vector containing only measurements in the oxygen A-band above sea (left panel), vegetation (middle panel), and snow (right panel) surfaces. The solid, dotted, and short-dashed lines correspond to the cloud fraction, cloud optical thickness, and cloud top pressure, respectively. The long-dashed line corresponds to the surface albedo at the oxygen A-band.

sea and vegetation surfaces. Measurements above snow surfaces only contain significant information about the cloud top pressure and less about the other cloud parameters. Instead, information about the surface albedo is retrieved from the measurements. This is because the effect on the measurements of such highly reflective surfaces is very similar to that of clouds.

[15] Figure 4 shows $\partial \hat{x}_i / \partial x_{a,i}$ corresponding to the retrieved parameters when, in addition to measurements in the oxygen A-band, measurements in the UV window are included. It can be seen that now all cloud parameters can be retrieved from the measurements with little dependence on a priori information. Thus, the information content is significantly increased by including UV measurements. Furthermore, information about the surface albedos is retrieved. Above sea surfaces, the dependence of the retrieved surface albedo in the UV window on its a priori value is low for low cloud fractions but increases rapidly for increasing cloud fraction. The surface albedo in the oxygen A-band window is determined almost entirely from the a priori values for all cloud fractions. Above

vegetation surfaces, the surface albedo in the oxygen A-band window is retrieved with only little dependence on a priori for all cloud fractions. The dependence on a priori for the surface albedo in the UV window is high but slightly decreases for decreasing cloud fractions. For other land surface types, excluding snow covered surfaces, the information content is similar to that of vegetation surfaces (not shown). Above snow covered surfaces, the surface albedos are almost fully obtained from the measurements with only little dependence on a priori. Here, the high surface albedo enhances the contribution of Rayleigh scattering in the UV close to the surface. Therefore, the effect of the surface reflection to the measurements in the UV is not similar to that of a cloud, in contrast to the situation at the oxygen A-band. This avoids the use of a priori albedo values of snow covered surfaces, which are highly uncertain, for the retrieval of cloud parameters. The linear dependences of the surface albedos are fully retrieved from the measurements in all cases and do not significantly depend on a priori values (not shown).
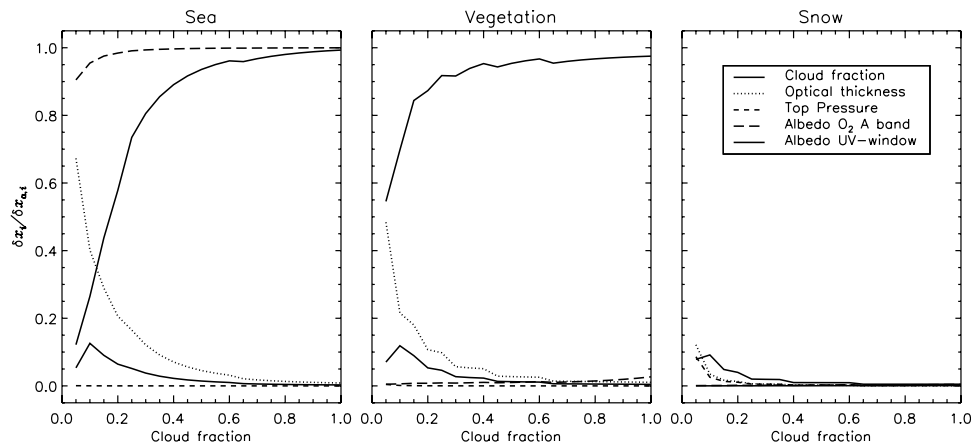

Figure 4. Same as Figure 3 but for a measurement vector containing measurements in the oxygen A-band and the UV window between 350–390 nm. The dotted-dashed line corresponds to the surface albedo in the UV window.
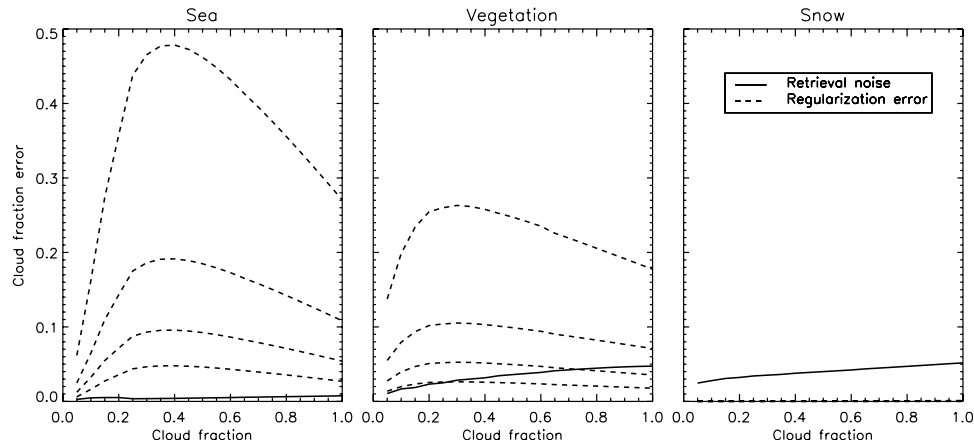
Figure 5. Retrieval noise (solid line) and regularization errors (dashed lines) on the retrieved cloud fraction for a measurement vector containing measurements in the oxygen A-band and the UV window above sea (left panel), vegetation (middle panel), and snow (right panel) surfaces. Regularization errors are shown for an error on the a priori surface albedo in the UV of 0.005, 0.01, 0.02, 0.05, corresponding to dashed lines with increasing errors, respectively.

[16] To summarize, using measurements in the UV in addition to the oxygen A-band for a large part solves the problem that cloud fraction and optical thickness cannot be independently retrieved from GOME and SCIAMACHY measurements.

3.2. Retrieval Noise and Regularization Errors

[17] The retrieval result given by (6) is affected by retrieval noise due to random measurement errors and by regularization errors due to uncertainties in the a priori information. Figure 5 shows the retrieval noise on the cloud fraction for measurements above sea, vegetation, and snow covered surfaces. Above sea surfaces, the retrieval noise on the retrieved cloud fraction is below 0.01 for all cloud fractions. Above vegetation surfaces and snow covered surfaces, the retrieval noise on the cloud fraction is below 0.05 and decreases slightly with increasing cloud fraction. The retrieval noise on the cloud optical thickness is shown in Figure 6. Above sea surfaces, the retrieval noise on the retrieved cloud optical thickness is below 1 for all cloud

fractions. Above vegetation and snow covered surfaces, the retrieval noise on the cloud optical thickness is below 2 and 1, respectively, for cloud fractions larger than 0.2 but increases to about 3 for lower cloud fractions.

[18] The regularization errors are dominated by errors due to errors on the a priori values of the surface albedos because the dependence of the cloud parameters on their a priori values is negligible for cloud fractions larger than 0.2. To give an indication of the regularization errors on the cloud parameters, Figures 5 and 6 also show the regularization errors due to errors of 0.005, 0.01, 0.02, and 0.05 on the a priori surface albedo in the UV. Above sea surfaces, a maximum occurs in the regularization errors on the cloud fraction at a cloud fraction of ~0.4. This is because, with increasing cloud fraction, on the one hand, the dependence of the retrieved surface albedo on its a priori value increases, while on the other hand, the contribution of the surface albedo to the measurements decreases (see Figure 4). The regularization errors on the cloud fraction are below 0.1 for errors on the a priori surface albedo in the UV below 0.01
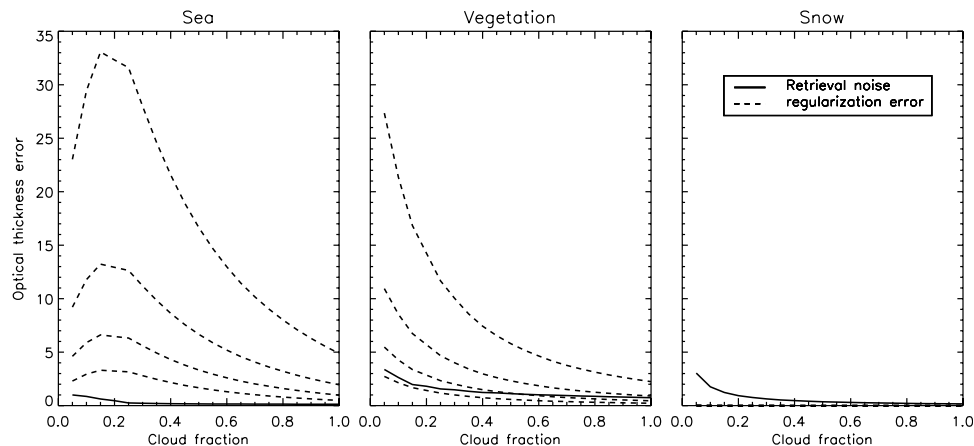

Figure 6. Same as Figure 5 but for the retrieval noise and regularization errors on the retrieved optical thickness.
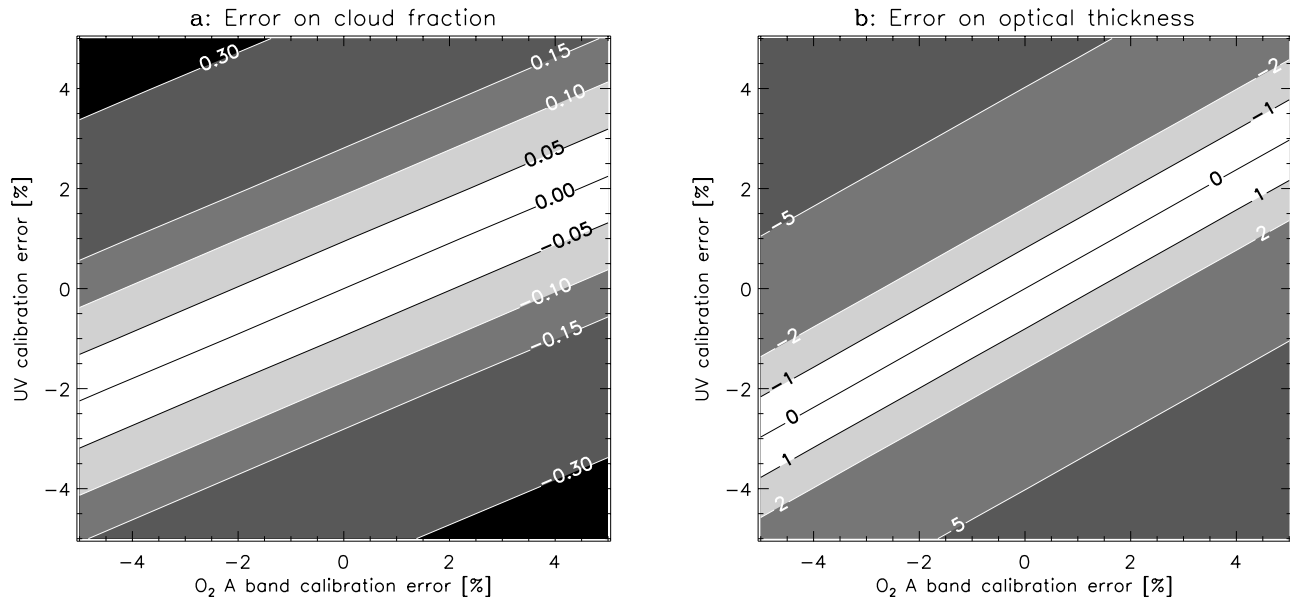
Figure 7. Absolute errors in the cloud fraction (a) and the cloud optical thickness (b) for retrievals above vegetation surfaces when calibration errors are added on the UV and oxygen A-band windows. Here, a cloud fraction of 0.5 is used in the simulated measurements.

and increase up to 0.5 for a priori surface albedo errors of 0.05. Above vegetation surfaces, the largest regularization errors on the cloud fraction occur around cloud fractions of 0.3. For errors on the a priori surface albedo in the UV below 0.01, the regularization errors are below 0.06. The regularization errors increase to 0.27 for a priori surface albedo in the UV errors of 0.05. Above snow covered surfaces, all regularization errors are negligible because here the surface albedos are obtained fully from the measurements. As shown in Figure 6, the regularization errors on the cloud optical thickness for retrievals above sea peak at a cloud fraction of 0.2. The regularization errors on the cloud optical thickness are below 7 for errors on the a priori surface albedo in the UV below 0.01 and increase up to 33 for a priori surface albedo errors of 0.05. Above vegetation surfaces, the regularization errors on the cloud optical thickness decrease with increasing cloud fraction. In contrast to the situation above sea surfaces, here no maximum occurs because the effect of the decreasing contribution of the surface albedo to the measurements with increasing cloud fraction is much larger than the effect due to the increase of dependence of the retrieved surface albedo on its a priori value. For a cloud fraction of 0.2, the errors are below 3 for errors on the a priori surface albedo in the UV below 0.01 and increase up to 15 for a priori surface albedo errors of 0.05. Again, all regularization errors are negligible for retrievals above snow covered surfaces. For errors on the a priori surface albedo in the oxygen A-band, similar results as shown in Figures 5 and 6 are obtained for retrievals above sea surfaces. For retrievals above vegetation and snow covered surfaces, these errors are negligible. The regularization error on the cloud top pressure due to errors in the a priori surface albedos up to 0.05 is generally below 5 hPa for all cases. In conclusion, accurate a priori information on surface albedo in both wavelength windows is needed for sea surfaces. Furthermore, for snow/ice-free land surfaces, accurate a priori information on surface albedo in the UV is required.

3.3. Sensitivity to Instrument Calibration

[19] GOME and SCIAMACHY measurements possibly have significant calibration errors [*Koelemeijer et al.*, 1998; *Tilstra et al.*, 2005]. Figure 7 shows the effect of calibration errors in the range $-5-5$ % on the retrieved cloud fraction and cloud optical thickness for retrievals over vegetation surfaces. Here, the relative calibration errors are assumed to be constant in the considered wavelength windows. Furthermore, a cloud fraction of 0.5 is assumed. As seen in Figure 7, small errors on the cloud fraction and optical thickness are obtained when the calibration in the two wavelength windows are correlated. Specifically, Figure 7a shows that the error on the cloud fraction is 0 when the calibration error in the oxygen A-band is about 2.5 times the calibration error in the UV. Figure 7b shows that, when the calibration error in the oxygen A-band is about 1.5 times the calibration error in the UV, the error on the optical thickness is 0. To obtain errors in the cloud fraction below 0.1 and in optical thickness below 2, the calibration error in the oxygen A-band has to be about twice the calibration error in the UV plus or minus 1%. When the calibration errors in the two wavelength windows differ considerably, large errors on the cloud fraction and optical thickness can occur. Moreover, in these cases, convergence of the inversion can become problematic. For decreasing cloud fractions, the regularization errors generally decrease. For example, for a calibration error of 2% at the oxygen A-band and no calibration error in the UV, the error on the cloud fraction decreases from 0.05 for a cloud fraction of 0.5 to 0.01 at a cloud fraction of 0.2. Furthermore, the error on the cloud optical thickness decreases with cloud fraction from 1.48 for a cloud fraction of 0.5 to 0.76 at a cloud fraction of 0.2.
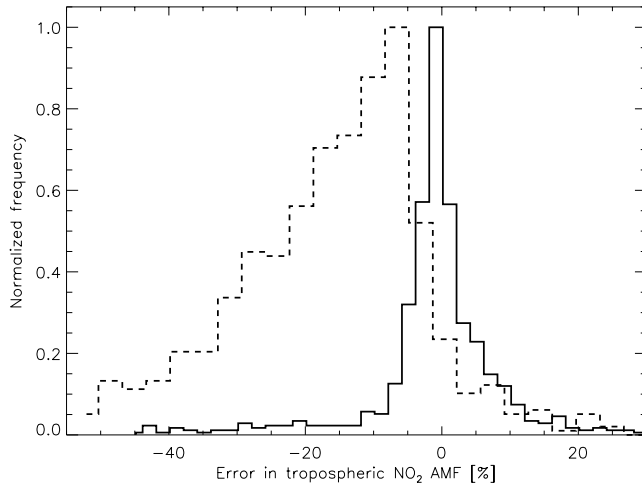
Figure 8. Histogram of the differences between the tropospheric NO_2 AMFs calculated for a random ensemble of cloud parameters and AMFs calculated for the corresponding retrieved cloud parameters (solid line) and effective cloud parameters (dashed line). The AMFs are calculated at 440 nm. Here a surface albedo of 0.05 is used.

[20] For retrievals over sea surfaces, similar errors are obtained. For retrievals above snow surfaces, the retrieval errors due to all calibration errors up to ±5% are significantly smaller and are generally below 2 in the optical thickness and below 0.05 in the cloud fraction. The retrieval errors on the cloud top pressure due to calibration errors are generally low for all surface types.

3.4. Relevance to Tropospheric NO_2 Retrievals

[21] In this section, the relevance of our cloud retrieval algorithm for the retrieval of the tropospheric NO_2 column in cloudy atmospheres is discussed. Tropospheric NO_2 columns derived with the Differential Optical Absorption Spectroscopy (DOAS) technique [*Platt*, 1994] are an important product of GOME, SCIAMACHY, and OMI measurements [e.g., *Beirle et al.*, 2003; *Richter et al.*, 2005]. These retrievals are particularly sensitive to clouds since the tropospheric NO_2 is generally below the cloud [*Schaub et al.*, 2006; *Wang et al.*, 2006].

[22] In the DOAS technique, first the reflectance spectrum is separated into a spectrally smooth part, modeled by a polynomial, and in a differential part from which a slant gas column (SCD) is retrieved. Then, this slant column is converted into a vertical column (VC) using an air mass factor (AMF), via

$$VC = \frac{SCD}{AMF} \quad (11)$$

Here the NO_2 AMF is given by

$$AMF = \frac{-\ln(R/R_0)}{\tau_{NO_2}} \quad (12)$$

where R and R_0 are the reflectances at the top of atmosphere at 440 nm with and without NO_2 absorption, respectively. Furthermore, τ_{NO_2} is the total NO_2 absorption optical

thickness. To calculate tropospheric NO_2 AMFs, we include NO_2 only in the lowest 2 km of the atmosphere. A NO_2 volume mixing ratio of 2.3 ppb is assumed, which corresponds to polluted situations. Furthermore, a surface albedo for of 0.05 is assumed for the AMF calculations.

[23] Here, we will investigate the errors in the AMF imposed by retrieval errors of our algorithm. Furthermore, we will show AMF errors that result from the use of effective cloud fractions and cloud top pressures retrieved from the oxygen A-band to demonstrate the advantage of our approach compared to approaches that only retrieve effective cloud parameters. For this, an ensemble of 600 cases is constructed with randomly chosen cloud fractions between 0 and 1, cloud optical thickness values between 2 and 30, and cloud top pressures between 400 and 600 hPa, above sea and vegetation surfaces. For these cases, measurements in the UV and oxygen A-band windows are simulated. Subsequently, the presented cloud retrieval algorithm is applied to these simulated measurements. For the cloud retrieval, an a priori cloud optical thickness of 5 and an a priori cloud top pressure of 500 hPa are taken. For the a priori cloud fraction, the effective cloud fraction is taken that corresponds to the priori cloud optical thickness. A random error of between −10% and +10% is assumed on the a priori surface albedos. In addition, effective cloud fractions and cloud top pressures are retrieved from the simulated measurements in the oxygen A-band, assuming a cloud optical thickness of 40. Then, for all cases, AMFs are calculated for the cloud parameters in the simulated measurements, the retrieved cloud parameters, and the effective cloud parameters. The cases for which our algorithm did not converge are removed from this study. Note that for all cases, all NO_2 is located below the height of the base of the cloud.

[24] Figure 8 shows histograms of the differences between the reference AMFs and those calculated with the retrieved cloud parameters and effective cloud parameters. The use of effective cloud parameters generally results in an underestimation of the AMF. The asymmetric distribution of AMF errors has a mean of −12.4%, a 68% confidence interval of ±10% and a significant wing toward negative errors. Using simulated measurements, *Wang et al.* [2006] also found a similar underestimation of the AMF for most solar zenith angles and cloud parameters. Thus, the use of effective cloud parameters generally leads to a significant overestimation of the tropospheric NO_2 column. A similar systematic overestimation was observed by *Schaub et al.* [2006] for tropospheric NO_2 column retrievals from GOME measurements in cloudy conditions when using effective cloud parameters obtained by FRESCO [*Koelemeijer et al.*, 2001]. When cloud parameters retrieved by the proposed algorithm are used, the errors in the AMF are symmetrically distributed around the mean of 0.4% with a 68% confidence interval of ±4.8%. Thus, the use of cloud parameters retrieved by our algorithm may be expected to solve the systematic overestimation of tropospheric NO_2 columns from GOME and SCIAMACHY measurements caused by effective cloud parameters in cloudy conditions.

4. Application to GOME Measurements

[25] In this section, we apply our retrieval algorithm for cloud parameters to GOME measurements. Here we use

3400 measurements spread evenly over the year 1997, above the European area, North Africa, and the Atlantic ocean. The areas and time range are chosen since it provides a data set with a considerable range of conditions. The retrieval results are compared with the effective cloud fractions and effective cloud pressures retrieved with the commonly used FRESCO algorithm [*Koelemeijer et al.*, 2001] from the same measurements. Furthermore, we compare our results with cloud fractions, cloud optical thicknesses, and cloud top pressures retrieved from ATSR-2 measurements using the Global Retrieval of ATSR Cloud Parameters and Evaluation (GRAPE) algorithm [*Watts et al.*, 1998; *Poulsen et al.*, 2005].

[26] In these comparisons, retrievals above snow covered surfaces, deserts, and sea surfaces with a significant contribution of sunglint are avoided, since both the GRAPE and FRESCO retrieval results are unreliable or unavailable for these cases [*Koelemeijer et al.*, 2001; *Poulsen et al.*, 2005].

4.1. Retrieval Input

[27] To model the GOME measurements, scattering and absorption cross-sections are calculated for atmospheric temperature and pressure profiles from the United Kingdom Met Office (UKMO) Stratospheric Assimilated data set at the locations closest to the center of each GOME measurement footprint. Furthermore, the surface elevation averaged over the GOME footprint is determined from the TerrainBase surface elevation database. To account for the variation in viewing angle within a GOME footprint, measurements are simulated for three viewing angles corresponding to the middle, west and east boundaries of the GOME footprint. The simulations are linearly interpolated and subsequently integrated over viewing angle. In the UV window, systematic structures due to the Ring effect [*Joiner et al.*, 2004; *Landgraf et al.*, 2004] and the 'undersampling' effect [*Chance et al.*, 2005; *van Deelen et al.*, 2007] appear in the GOME measurements. These structures are partly removed by fitting theoretically calculated Ring spectra [*Landgraf et al.*, 2004] and "undersampling" effect correction spectra to the data in addition to the cloud parameters. For these spectra, an amplitude and a wavelength shift and squeeze are fitted.

[28] The a priori surface albedos are obtained from the monthly $1° \times 1°$ resolution Minimum Lambertian-Equivalent Reflectivity (MLER) database determined from cloud-free GOME observations [*Koelemeijer et al.*, 2003]. For this purpose, the MLER database gridboxes overlapping the GOME footprint are averaged, weighted by the amount of overlap. For GOME footprints containing more than 95% sea surfaces, the Fresnel reflection on the waves is characterized by a modeled ocean reflection matrix, as discussed in section 2.1. For this, the required wind speedwindspeed is taken from re-analysis data of the European Center for Medium range Weather Forecasting (ECMWF) averaged over the GOME footprint.

[29] The pressure difference between the top and bottom of the cloud is fixed to 200 hPa, since this is a common geometrical thickness for middle- and low-level clouds [*Wang et al.*, 2000]. The a priori cloud optical thickness is set to 5, which is roughly the mean global value for middle- and low-level clouds [*Rossow and Schiffer*, 1999]. The a priori values of the cloud fraction are the effective cloud fractions corresponding to the a priori cloud optical thickness. The a priori cloud top pressures are taken from data from the FRESCO algorithm [*Koelemeijer et al.*, 2001]. It is important to note however that the cloud fraction and cloud top pressure retrieved by our algorithm only minimally depend on their a priori values, as discussed in section 3.1.

4.2. Comparison to FRESCO Results

[30] In the FRESCO algorithm, clouds are approximated by reflecting boundaries with a Lambertian albedo of 0.8. Furthermore, surface albedos are taken from *Koelemeijer et al.* [2003]. With these assumptions, effective cloud fractions and effective cloud pressures are retrieved from measurements in the oxygen A-band. Figure 9 shows the cloud fractions retrieved by our algorithm compared to the effective cloud fractions obtained by FRESCO (version 3). For clouds with a cloud fraction higher than 0.2 and an optical thickness between 30 and 60 (diamonds), the cloud fraction retrieved using our algorithm and effective cloud fractions from FRESCO agree well. For optically thinner and thicker clouds, the cloud fractions obtained by our algorithm are generally higher and lower, respectively, than the effective cloud fractions from FRESCO. This is as expected since clouds with optical thickness around 40 have Lambertian equivalent albedos around 0.8, which is the value assumed in the FRESCO algorithm. When the cloud optical thickness is lower or higher than 40, this is compensated in FRESCO by respectively increasing or decreasing the effective cloud fraction. Thus, for cloud fractions larger than 0.2, the cloud fractions retrieved by our algorithm are consistent with the effective cloud fractions retrieved by FRESCO, given the definition of the effective cloud fraction in FRESCO. For cloud fractions lower than 0.2 above land, often the effective cloud fractions from FRESCO are higher than the cloud fractions retrieved by our algorithm. This is probably due to a difference in the surface albedo in the oxygen A-band window assumed by the FRESCO algorithm and that retrieved by our algorithm.

[31] Figure 10 shows the histogram of the differences between cloud top pressures retrieved by our algorithm and the effective cloud pressures from FRESCO. These differences have a median of -59 (±40) hPa or 0.77 (±0.70) km, where the value between brackets indicates the 68% confidence interval. The systematic difference depends on the optical thickness of the clouds included in the comparison, namely the difference increases for decreasing cloud optical thickness. This systematic difference is probably due to the neglect of scattering and absorption within the cloud and the transmission of light through the cloud by the FRESCO algorithm [*Koelemeijer et al.*, 2001].

4.3 Comparison to ATSR-2 Retrievals

[32] In this subsection, our retrieval results are compared with cloud parameters retrieved from ATSR-2, which is on the same platform as GOME. ATSR-2 has a subsatellite footprint size of 1×1 km^2, and its swath entirely overlaps with the footprints of GOME for the used observations.

[33] We use ATSR-2 cloud parameters retrieved by the GRAPE algorithm, version 1 [*Watts et al.*, 1998; *Poulsen et al.*, 2005; http://www-atm.physics.ox.ac.uk/group/grape/]. At the time of preparation of this paper, version 2 GRAPE data were not yet available. In the GRAPE algorithm, first
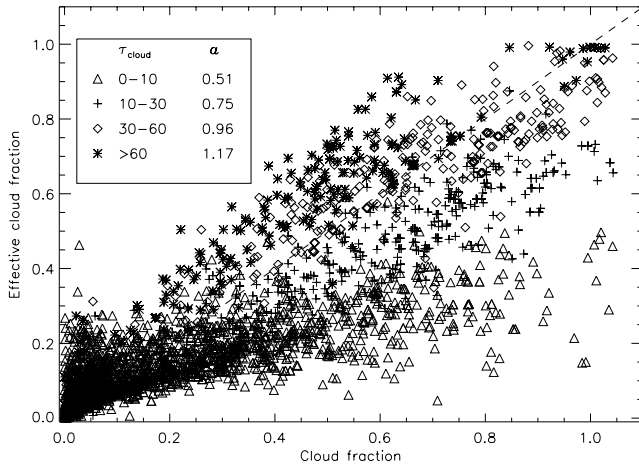
Figure 9. Comparison of retrieved cloud fractions using the presented algorithm and the effective cloud fractions retrieved by the FRESCO algorithm. The different symbols correspond to selected ranges in retrieved cloud optical thickness τ_{cloud}. Furthermore, a represents the slopes of the linear functions fitted through the data in the selected ranges and the origin.

cloudy ATSR-2 pixels are identified using a cloudfilter. For these cloudy pixels, then an optimal estimation procedure is used to estimate cloud fraction, cloud optical thickness, and cloud top pressure as well as the effective radius of the cloud particles, using measurements of the 0.67, 0.87, 1.6, 11 and 12 μm channels on ATSR-2. Furthermore, the cloud phase (water or ice) is determined.

[34] To compare the retrievals on the GOME spatial resolution, the cloud fractions retrieved by GRAPE for ATSR-2 measurements within a GOME footprint are averaged. Furthermore, the GRAPE cloud top pressures and optical thickness values within a GOME footprint are averaged weighted by the GRAPE cloud fraction. ATSR-2 measurements for which the GRAPE algorithm retrieved a cloud optical thickness below 2 are considered as clear sky,
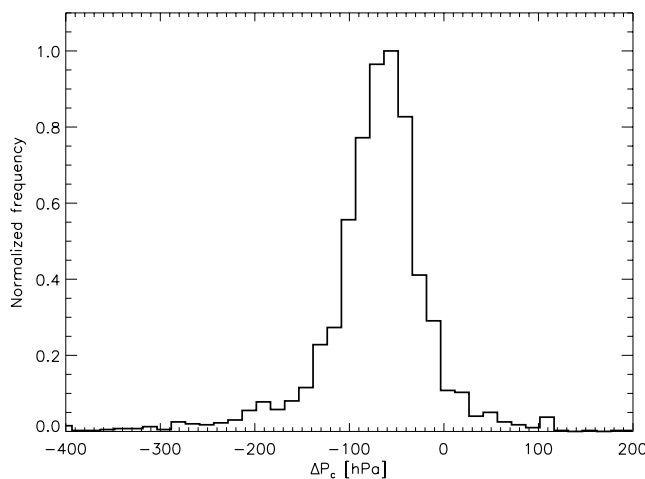
since most of these cases are either thin cirrus clouds for which GOME is insensitive or pixels falsely identified as cloudy by the strict cloudfilter used by GRAPE.

[35] Figures 11 and 12 show histograms of the differences between the cloud fractions and optical thickness, respectively, retrieved by our algorithm and those from ATSR-2. For the comparisons of the optical thickness, all cases with a cloud fraction lower than 0.05 are excluded. The cloud fraction and optical thickness values retrieved by our algorithm compare well to the corresponding ATSR-2 values. Here, the differences between the GOME and ATSR-2 values have median values of −0.01 (±0.11) for the cloud fraction and 2.5 (±7.5) for the cloud optical thickness. No obvious dependence of these results on geometry, location, or surface albedos is found. Retrievals performed for a fixed cloud geometrical thickness of 100 hPa instead of 200 hPa only yield mean differences in cloud fraction and cloud optical thickness of less than 0.01 and 0.5, respectively.

[36] The distributions of the differences in cloud fraction and cloud optical thickness both show significant wings, where the cloud fractions are underestimated by our algorithm as compared to the ATSR-2 values, and at the same time the cloud optical thickness values are overestimated. This is the situation for about 15% of all cases above land. The standard deviation of the ATSR-2 optical thickness values within the GOME pixels for these cases are about 20, which is about twice as high as compared to the average value. This indicates that the obtained biases for these cases could be due to the presence of horizontally inhomogeneous clouds. Furthermore, multilayered clouds could cause these biases. This is indicated by the fact that, for these cases, the cloud top pressures retrieved by ATSR-2 are on average about 67 hPa lower than those retrieved by GOME. This difference is expected for multilayered clouds since ATSR-2 is mostly sensitive for the top layer, while GOME retrieves a higher cloud top pressure in these cases [*Rozanov et al.*, 2004]. It is important to note that the χ^2 values of the spectral fit to the measurements for these cases are very
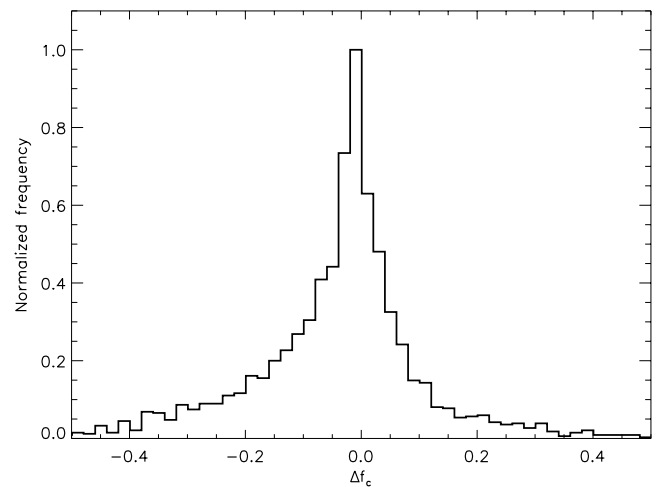

Figure 10. Histogram of ΔP_c defined as the cloud top pressures retrieved by our algorithm minus the effective cloud pressures from FRESCO. In this comparison, all cases with a cloud fraction lower than 0.05 are excluded.

Figure 11. Histogram of Δf_c defined as cloud fractions retrieved from GOME measurements using the presented algorithm minus those retrieved from ATSR-2 measurements using the GRAPE algorithm averaged over the corresponding GOME footprint.
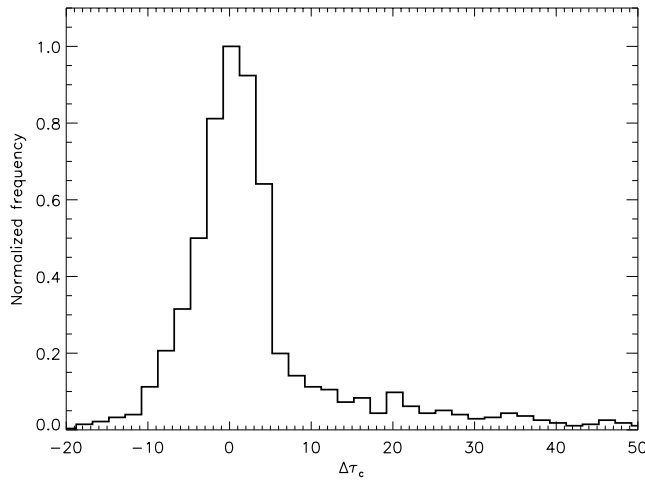
Figure 12. Similar to Figure 11 but for $\Delta\tau_c$ defined as the cloud optical thickness retrieved by our algorithm minus the ATSR-2 values. Here all cases with a cloud fraction lower than 0.05 are excluded.

similar to those of other cases. This suggests that these retrieved parameters may still be very useful for the retrieval of trace gas abundances from the corresponding GOME measurements. Wavelength-dependent effects due to inhomogeneous or multilayered clouds are partly taken into account since cloud parameters are retrieved that describe the spectrum in both the UV and the oxygen A-band.

[37] Figure 13 shows the histogram of the differences between the cloud top pressure retrieved by our algorithm and the ATSR-2 values. Again, all cases with a cloud fraction lower than 0.05 are excluded. The differences between the cloud top pressure retrieved by our algorithm and the ATSR-2 values have a median of −33 (±111) hPa or 0.4 (±1.6) km. No obvious dependence of these results on geometry, location, or surface albedos is found. *Rozanov et al.* [2006] find a similar bias and spread of 0.6 (±1.8) km between cloud top pressures derived from ATSR-2 and those derived from fully clouded GOME measurements
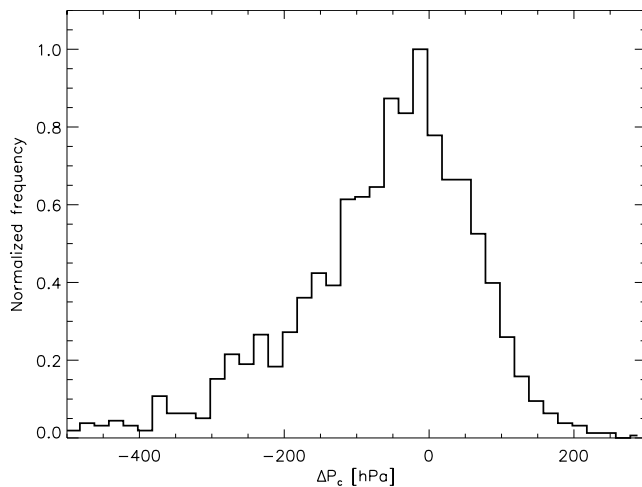
with the Semi-analytical Cloud Retrieval Algorithm (SACURA) [*Rozanov and Kokhanovsky*, 2004]. Thus, the retrieved cloud top pressures can be assumed to be consistent to those of SACURA. *Rozanov and Kokhanovsky* [2004] showed that the cloud top pressure derived from the oxygen A-band depends on the assumed geometrical thickness of the cloud. When in our algorithm the cloud geometrical thickness is fixed at 100 hPa instead of 200 hPa, the mean retrieved cloud top pressure is about 50 hPa higher (or 0.8 km lower). Thus, the negative bias of the retrieved cloud top pressure compared to the ATSR-2 values could be due to an overestimation of the cloud geometrical thickness. To account for this, the geometrical thickness of the cloud layer could in the theory be retrieved from the measurements as well. However, in practice this often leads to unphysical retrieval results with cloud bases under the ground surface due to the presence of multilayered or vertically inhomogeneous clouds [*Rozanov and Kokhanovsky*, 2004]. The negative bias of the retrieved cloud top pressure compared to the ATSR-2 values could also be due to systematic overestimation of the cloud top pressures by ATSR-2, since cloud top pressures determined using infrared brightness temperature measurements, as in GRAPE, are known to be biased toward higher cloud top pressures [*Rossow and Schiffer*, 1999; *Sherwood et al.*, 2004]. Here, the difference between the cloud top pressures from GOME and ATSR-2 clearly depends on the optical thickness of the cloud, especially above land. For example, for clouds with an optical thickness higher than 40, the cloud top pressures retrieved by our algorithm are on average about 95 hPa higher (or 1.27 km lower) than the ATSR-2 cloud top pressures. However, when only clouds with an optical thickness below 10 are compared, the cloud top pressures retrieved by our algorithm are on average about 85 hPa lower (or 1.09 km higher) than the ATSR-2 cloud top pressures. It is not clear whether this dependency on optical thickness is caused by GRAPE or by our algorithm.

4.4. Spectral Fitting Residuals

[38] Figure 14 shows the obtained mean spectral fitting residual in the UV window and its standard deviation.

Figure 13. Similar to Figure 11 but for ΔP_c defined as the cloud top pressures retrieved by our algorithm minus the ATSR-2 cloud top pressures. Only clouds with cloud fractions larger than 0.05 are included in this histogram.
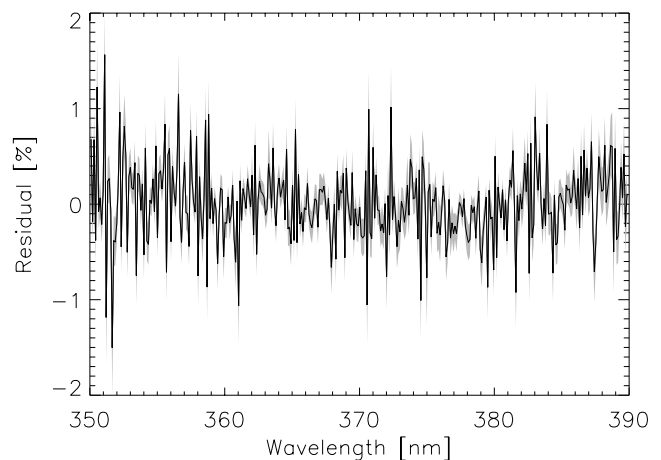

Figure 14. Mean spectral fit residual between forward model and GOME measurements in the UV window. The standard deviation around the mean is indicated with the grey area.
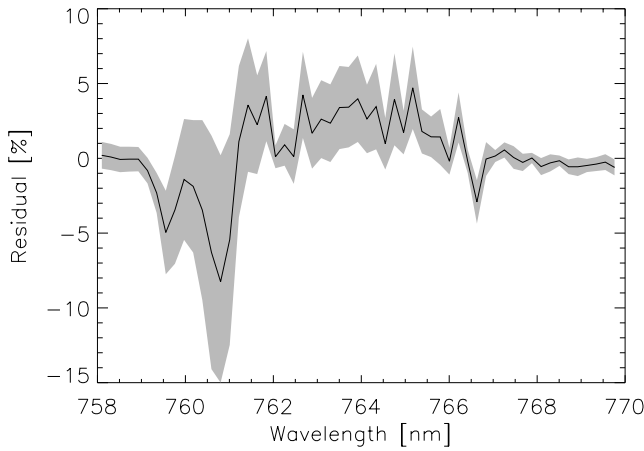
Figure 15. Same as Figure 14 but for the oxygen A-band.

Averaged over the whole wavelength range in this window, the mean spectral fitting residual is 0.005%, and the mean of the standard deviations is 0.21%. The residuals show no significant broad spectral behavior, but many spectral fine structures are apparent. Similar fine structures were also found by *Joiner et al.* [2004] analyzing GOME data. These residuals are probably due to insufficient correction of the "undersampling" effect [*van Deelen et al.*, 2007] and the Ring effect [*Joiner et al.*, 2004; *Landgraf et al.*, 2004].

[39] In Figure 15, the obtained mean spectral fitting residual in the oxygen A-band and its standard deviation are shown. In this window, the mean spectral fitting residual and the mean standard deviation averaged over the wavelength range are −0.24% and 2.1%, respectively. Especially around the deep R-branch at 761 nm, the spectral fitting residual and the standard deviation are high. The mean residuals are very similar to those found by *van Diedenhoven et al.* [2005] retrieving surface pressures from SCIA-MACHY and GOME measurements in the oxygen A-band. This indicates that many of these structures in the mean residuals may be due to errors in the spectroscopy data [*Chance*, 1997; *Rothman et al.*, 2005], assumption of the spectral lineshapes [*Yang et al.*, 2005; *Tran et al.*, 2006], and insufficient knowledge of the instrument response function. The large spread and the large residual structure around 761 nm could be related to approximations made in the cloud model such as the fixed geometrical thickness and the use of a homogeneous cloud layer.

[40] The systematic structures in the residuals could lead to unaccounted biases in the retrieval.

5. Conclusions

[41] In this paper, we have presented a new method to retrieve information about cloud fraction, cloud optical thickness, and cloud top pressure from GOME and SCIA-MACHY measurements. Additionally, information on surface albedo is retrieved. The method makes use of measurements at the oxygen A-band from 758 to 770 nm and in the UV from 350 to 390 nm. The inversion is based on the Phillips−Tikhonov regularization method. An advantage of this approach in comparison to common approaches using only the oxygen A-band is that, in addition to the cloud top pressure, information about both the cloud fraction and cloud optical thickness can be retrieved, instead of only an

effective cloud fraction. The retrieved cloud parameters are relevant for the retrieval of trace gas abundances in cloudy atmospheres.

[42] It was shown that measurements at the oxygen A-band alone do not contain sufficient information for the independent retrieval of the cloud fraction, cloud optical thickness, and cloud top pressure. Adding the UV window allows to retrieve significant information about all three cloud parameters. Furthermore, information about the surface reflection can be obtained from these measurements. The UV window adds information on the cloud fraction because in the clear sky part of the measurement, the spectrum is dominated by Rayleigh scattering, which has a strong wavelength dependence. Due to the significant differences between the spectral signature of Rayleigh scattering and that of scattering by cloud particles, the UV window is especially sensitive to the cloud fraction.

[43] Using simulated measurements, it was shown that the use of effective cloud fractions and cloud top pressures leads to a significant systematic underestimation of the tropospheric NO_2 AMF in cloudy atmospheres, which can be avoided using cloud parameters retrieved by the proposed algorithm.

[44] The cloud retrieval algorithm was applied to GOME data, and the results were compared to effective cloud parameters from the FRESCO algorithm [*Koelemeijer et al.*, 2001]. In the FRESCO algorithm, clouds are approximated by reflecting boundaries with a Lambertian albedo of 0.8. The cloud fractions retrieved by our algorithm are consistent with the effective cloud fractions retrieved by FRESCO, given the definition of the effective cloud fraction in FRESCO. Also, the cloud top pressures retrieved by our algorithm generally agree well with the effective cloud pressures retrieved by FRESCO with a 68% confidence interval of ±40 hPa, although an offset of about −60 hPa is observed. Furthermore, our results were compared to cloud parameters retrieved from ATSR-2 measurements by the GRAPE algorithm. The distributions of the differences between the cloud fractions, cloud optical thickness, and cloud top pressures retrieved by our algorithm and the corresponding ATSR-2 values have median values of −0.01 (±0.11), 2.5 (±7.5), and −33 (±111) hPa, respectively.

Appendix A: The Phillips−Tikhonov Regularization Method

[45] The Phillips−Tikhonov regularization method [*Phillips*, 1962; *Tikhonov*, 1963] can be used to reduce the effect of measurement noise in ill-posed inverse problems. In the Phillips−Tikhonov regularization method, the solution $\hat{\mathbf{x}}_{\mathrm{reg}}$ is given by the least squares solution with an additional side constraint, viz.

$$\hat{\mathbf{x}}_{\mathrm{reg}} = \min_{\mathbf{x}} \left(\left\| \mathbf{S}_y^{-\frac{1}{2}} (\mathbf{F}(\mathbf{x}) - \mathbf{y}) \right\|^2 + \gamma \left\| \mathbf{\Gamma}\mathbf{x} \right\|^2 \right), \quad (A1)$$

where $\mathbf{\Gamma}$ is a diagonal matrix that contains weighting factors for the different state vector elements in the side constraint, and γ is the regularization parameter. In its linear approximation, the solution $\hat{\mathbf{x}}_{\mathrm{reg}}$ in (A1) can be written as

$$\hat{\mathbf{x}}_{\mathrm{reg}} = \mathbf{D}\,\tilde{\mathbf{y}} \quad (A2)$$

where $\tilde{\mathbf{y}} = \mathbf{y} - \mathbf{F}(\mathbf{x}) + \mathbf{K}\mathbf{x}$ and $\mathbf{D}$ is the contribution matrix defined by

$$\mathbf{D} = (\mathbf{K}^T \mathbf{S}_y^{-1} \mathbf{K} + \gamma \mathbf{\Gamma})^{-1} \mathbf{K}^T \mathbf{S}_y^{-1}, \qquad (A3)$$

where the superscript T denotes the transposed matrix. Since the weighted norm of the state vector is a quantity that is very sensitive to noise contributions, these contributions are reduced by introducing the side constraint in (A1). For the Phillips–Tikhonov solution, γ should be chosen such that the minimizations of the weighted least squares norm $\|\mathbf{S}_y^{\frac{1}{2}}(\mathbf{F}(\mathbf{x}) - \mathbf{y})\|$ and the weighted solution norm $\|\mathbf{\Gamma}\mathbf{x}\|$ in (A1) are well balanced. Such a value for γ is found from the so-called L-curve [*Hansen and O'Leary*, 1993; *Hansen*, 1992].

[46] The weighting factors in the matrix $\mathbf{\Gamma}$ are defined relative to the elements of the corresponding state vector of the iteration step under consideration, making $\mathbf{\Gamma}\mathbf{x}$ dimensionless. Increasing the weighting factor in $\mathbf{\Gamma}$ for a certain parameter decreases the information about this parameter that is obtained from the measurements, while for other parameters, more information is taken from the measurements. Since the a priori information about the surface albedos in our retrieval scheme is more accurate than a priori information of cloud parameters and because we focus our retrieval scheme on the retrieval of cloud parameters, we increase the weights in $\mathbf{\Gamma}$ corresponding to the surface albedos by a factor of 10 relative to the weights corresponding to the cloud parameters.

[47] Owing to the inclusion of the side constraint in (A1), the state vector $\hat{\mathbf{x}}_{\text{reg}}$ retrieved using (A1) does not represent an estimate of the true state vector $\mathbf{x}_{\text{true}}$, but its elements represent weighted averages of the elements of $\mathbf{x}_{\text{true}}$. Since $\mathbf{x}_{\text{true}}$ contains several different cloud and surface parameters, the weighted averages in $\hat{\mathbf{x}}_{\text{reg}}$ have a limited physical meaning. Therefore we include information from an a priori state vector $\mathbf{x}_a$ in the solution to make it a meaningful estimate of $\mathbf{x}_{\text{true}}$, viz.

$$\hat{\mathbf{x}} = \hat{\mathbf{x}}_{\text{reg}} + (\mathbf{I} - \mathbf{A})\mathbf{x}_a. \qquad (A4)$$

Furthermore, $\mathbf{A}$ is the averaging kernel [*Rodgers*, 2000], given by

$$\mathbf{A} = \frac{\partial \hat{\mathbf{x}}}{\partial \mathbf{x}_{\text{true}}} = \left(\mathbf{K}^T \mathbf{S}_y^{-1} \mathbf{K} + \gamma \mathbf{\Gamma}\right)^{-1} \mathbf{K}^T \mathbf{S}_y^{-1} \mathbf{K}. \qquad (A5)$$

For more details about the Phillips–Tikhonov regularization method, we refer to the paper of *Hasekamp and Landgraf* [2005].

Appendix B: The Levenberg–Marquardt Method

[48] The Levenberg–Marquardt method [*Levenberg*, 1944; *Marquardt*, 1964] can be used to improve the convergence of a nonlinear iterative inversion problem. Applying the Levenberg–Marquardt method in combination with the Phillips–Tikhonov method described in Appendix A, the solution $\hat{\mathbf{x}}_{n+1}$ for iteration step $n + 1$ is given by [*Rodgers*, 2000]

$$\hat{\mathbf{x}}_{n+1} = \hat{\mathbf{x}}_n + [\mathbf{\Gamma}(\gamma + \lambda) + \mathbf{K}_n^T \mathbf{S}_y^{-1} \mathbf{K}_n]^{-1} \\ [\mathbf{K}_n^T \mathbf{S}_y^{-1} (\mathbf{y} - \mathbf{F}(\mathbf{x}_n)) - \gamma \|\mathbf{\Gamma}(\hat{\mathbf{x}}_n - \mathbf{x}_\mathbf{a})\|], \qquad (B1)$$

where the parameter λ is introduced to limit the change in $\mathbf{x}$ in each iteration step. We follow the procedure by *Press et al.* [1992] for the choice of λ. When the Levenberg–Marquardt procedure has converged, $\lambda = 0$ and the Phillips–Thikhonov regularization described in Appendix A is used. For more details about the Levenberg–Marquardt method, we refer to the study by *Rodgers* [2000].

[49] Although the Levenberg–Marquardt method improves the convergence of the iterative inversion problem discussed in section 2.2, still many iterations are needed due to the strong nonlinearity of the problem. This nonlinearity is mainly due to the strong dependence of the Jacobian matrix $\mathbf{K}$ on the cloud fraction. To reduce the computational effort, the forward models $\mathbf{F}_{\text{cloud}}$ and $\mathbf{F}_{\text{clear}}$ in (2) are approximated by their linear approximations

$$\tilde{\mathbf{F}}_{\text{cloud}}(\mathbf{x}^{\text{cloud}}) \approx \mathbf{F}_{\text{cloud}}(\mathbf{x}_0^{\text{cloud}}) + \mathbf{K}_{\text{cloud}}(\mathbf{x}_0^{\text{cloud}})[\mathbf{x}^{\text{cloud}} - \mathbf{x}_0^{\text{cloud}}] \text{ and}$$
$$\tilde{\mathbf{F}}_{\text{clear}}(\mathbf{x}^{\text{clear}}) \approx \mathbf{F}_{\text{clear}}(\mathbf{x}_0^{\text{clear}}) + \mathbf{K}_{\text{clear}}(\mathbf{x}_0^{\text{clear}})[\mathbf{x}^{\text{clear}} - \mathbf{x}_0^{\text{clear}}], \qquad (B2)$$

respectively, where $\mathbf{x}^{\text{cloud}}$ is a subset of the state vector containing surface and cloud parameters, and $\mathbf{x}^{\text{clear}}$ is a subset containing only surface parameters. Furthermore, $\mathbf{x}_0^{\text{cloud}}$ and $\mathbf{x}_0^{\text{clear}}$ are the sets of parameters for which the exact calculation of $\mathbf{F}_{\text{clear}}$ and $\mathbf{F}_{\text{cloud}}$ were performed. $\mathbf{K}_{\text{cloud}}$ and $\mathbf{K}_{\text{clear}}$ are the Jacobian matrices for the cloudy part and clear sky part of the measurement footprint, respectively. Using (B2), the forward model $\mathbf{F}$ can be approximated by

$$\tilde{\mathbf{F}} = (1 - f_c) \, \tilde{\mathbf{F}}_{\text{clear}} + f_c \, \tilde{\mathbf{F}}_{\text{cloud}}. \qquad (B3)$$

The derivative of $\tilde{\mathbf{F}}$ with respect to the cloud fraction f_c is

$$\frac{\partial \tilde{\mathbf{F}}}{\partial f_c} = \tilde{\mathbf{F}}_{\text{cloud}} - \tilde{\mathbf{F}}_{\text{clear}}. \qquad (B4)$$

Furthermore, the derivatives of $\tilde{\mathbf{F}}$ with respect to the other parameters x_i are

$$\frac{\partial \tilde{\mathbf{F}}}{\partial x_i} = (1 - f_c) \frac{\partial \mathbf{F}_{\text{clear}}}{\partial x_i}(\mathbf{x}_0^{\text{clear}}) + f_c \, \frac{\partial \mathbf{F}_{\text{cloud}}}{\partial x_i}(\mathbf{x}_0^{\text{cloud}}). \qquad (B5)$$

Thus, using (B2), (B3), (B4), and (B5), the forward model and the Jacobian matrix at state vector $\mathbf{x}$ can be approximated using exact forward model calculations at state vector $\mathbf{x}_0$ without any significant computational effort. When the iteration using this approximate forward model has converged, a new exact forward model calculation is performed to initiate the next iteration.

References

Bednarz, F. (Ed.) (1995), *Global Ozone Monitoring Experiment users manual*, European Space Research and Technology Centre (ESTEC), Noordwijk, The Netherlands.

Beirle, S., U. Platt, M. Wenig, and T. Wagner (2003), Weekly cycle of NO$_2$ by GOME measurements: A signature of anthropogenic sources, *Atmos. Chem. Phys.*, 3, 2225–2232.

Bovensmann, H., J. P. Burrows, M. Buchwitz, J. Frerick, S. Noel, V. V. Rozanov, K. V. Chance, and A. P. H. Goede (1999), Sciamachy: Mission objectives and measurement modes, *J. Atmos. Sci.*, 56, 127–150.

Bucholtz, A. (1995), Rayleigh-scattering calculations for the terrestrial atmosphere, *Appl. Opt.*, 34, 2765–2773.

Burrows, J. P., et al. (1999), The Global Ozone Monitoring Experiment (GOME): mission concept and first scientific results., *J. Atmos. Sci.*, 56, 151–175.

Chance, K. (1997), Improvement of the O_2 A band spectroscopic database for satellite-based cloud detection, *J. Quant. Spectrosc. Radiat. Transfer*, 58, 375–378.

Chance, K., T. P. Kurosu, and C. E. Sioris (2005), Undersampling correction for array detector-based satellite spectrometers, *Appl. Opt.*, 44, 1296–1304.

Cox, C., and W. Munk (1954), Statistics of the sea surfaces derived from sun glitter, *J. Mar. Res.*, 13, 198–227.

de Rooij, W. A., and C. C. A. H. van der Stap (1984), Expansion of Mie scattering matrices in generalized spherical functions, *Astr. and Astrophys.*, 131, 237–248.

Greenblatt, G. D., J. J. Orlando, J. B. Burkholder, and A. R. Ravishankara (1990), Absorption measurements of oxygen between 330 and 1140 nm, *J. Geophys. Res.*, 95, 18,577–18,582.

Grzegorski, M., M. Wenig, P. Stammes, N. Fournier, and T. Wagner (2006), The Heidelberg iterative cloud retrieval utilities (HICRU) and its application to GOME data, *Atmos. Chem. Phys.*, 6, 4461–4476.

Hansen, P. (1992), Analysis of discrete ill posed problems by means of the L-curve, *SIAM Rev.*, 34, 561–580.

Hansen, P., and D. O'Leary (1993), The use of the L-curve in the regularization of discrete ill posed problems, *SIAM J. Sci. Comput.*, 14, 1487–1503.

Hansen, J. E., and L. D. Travis (1974), Light scattering in planetary atmospheres, *Sp. Sci. Rev.*, 16, 527–610.

Hasekamp, O. P., and J. Landgraf (2002), A linearized vector radiative transfer model for atmospheric trace gas retrieval, *J. Quant. Spectrosc. Radiat. Transfer*, 75, 221–238.

Hasekamp, O. P., and J. Landgraf (2005), Retrieval of aerosol properties over the ocean from multispectral single-viewing-angle measurements of intensity and polarization: Retrieval approach, information content, and sensitivity study, *J. Geophys. Res.*, 110(D9), D20207, doi:10.1029/2005JD006212.

Hasekamp, O. P., J. Landgraf, and R. van Oss (2002), The need of polarization modeling for ozone profile retrieval from backscattered sunlight, *J. Geophys. Res.*, 107(D23), 4692, doi:10.1029/2002JD002387.

Joiner, J., A. P. Vasilkov, D. E. Flittner, J. F. Gleason, and P. K. Bhartia (2004), Retrieval of cloud pressure and oceanic chlorophyll content using Raman scattering in GOME ultraviolet spectra, *J. Geophys. Res.*, 109, D01109, doi:10.1029/2003JD003698.

Koelemeijer, R. B. A., and P. Stammes (1999), Effects of clouds on ozone column retrieval from GOME UV measurements, *J. Geophys. Res.*, 104(D7), 8281–8294, doi:10.1029/1999JD900012.

Koelemeijer, R. B. A., P. Stammes, and P. Watts (1998), Comparison of visible calibrations of GOME and ATSR-2, *Remote Sens. Environ.*, 63, 279–288.

Koelemeijer, R. B. A., P. Stammes, J. W. Hovenier, and J. F. de Haan (2001), A fast method for retrieval of cloud parameters using oxygen a band measurements from the Global Ozone Monitoring Experiment, *J. Geophys. Res.*, 106(D4), 3475–3490, doi:10.1029/2000JD900657.

Koelemeijer, R. B. A., J. F. de Haan, and P. Stammes (2003), A database of spectral surface reflectivity in the range 335–772 nm derived from 5.5 years of GOME observations, *J. Geophys. Res.*, 108(D2), 4070, doi:10.1029/2002JD002429.

Krijger, J., M. van Weele, I. Aben, and R. Frey (2007), Technical note: The effect of sensor resolution on the number of cloud-free observations from space, *Atmos. Chem. Phys.*, 7, 2881–2891.

Kurosu, T., K. Chance, and R. Spurr (1999), CRAG-Cloud Retrieval Algorithm for the European Space Agency's Global Ozone Monitoring Experiment, in *Proceedings of the European Symposium of Atmospheric Measurements from Space (ESAMS)*, pp. 513–521.

Kuze, A., and K. V. Chance (1994), Analysis of cloud top height and cloud coverage from satellites using the O_2 A and B bands, *J. Geophys. Res.*, 99, 14,481–14,491.

Landgraf, J., O. P. Hasekamp, R. van Deelen, and I. Aben (2004), Rotational Raman scattering of polarized light in the Earth atmosphere: A vector radiative transfer model using the radiative transfer perturbation theory approach, *J. Quant. Spectrosc. Radiat. Transfer*, 87, 399–433.

Levelt, P. F., G. H. J. van den Oord, M. R. Dobber, A. Malkki, H. Visser, J. de Vries, P. Stammes, J. O. V. Lundell, and H. Saari (2006), The ozone–monitoring instrument, *IEEE Trans. Geosc. Remote Sens.*, 44(5), 1093–1101.

Levenberg, K. (1944), A method for the solution of certain nonlinear problems in least squares, *Q. Appl. Math.*, 2, 164.

Liu, X., M. J. Newchurch, R. Loughman, and P. K. Bhartia (2004), Errors resulting from assuming opaque Lambertian clouds in TOMS ozone retrieval, *J. Quant. Spectrosc. Radiat. Transfer*, 85, 337–365.

Marquardt, D. W. (1964), An algorithm for least-squares estimation of nonlinear parameters, *SIAM J. Appl. Math.*, 11, 431.

Marshak, A., A. Davis, W. Wiscombe, and G. Titov (1995), The verisimilitude of the independent pixel approximation used in cloud remote sensing, *Remote Sens. Environ.*, 52, 71–78.

Mishchenko, M. I., and L. D. Travis (1997), Satellite retrieval of aerosol properties over the ocean using polarization as well as intensity of reflected sunlight, *J. Geophys. Res.*, 102(D14), 16989–17014, doi:10.1029/96JD02425.

Phillips, P. (1962), A technique for the numerical solution of certain integral equations of the first kind, *J. Assoc. Comput. Mach.*, 9, 84–97.

Platt, U. (1994), Differential optical absorption spectroscopy (DOAS) in Air monitoring by spectrometric techniques, John Wiley & sons, New York.

Poulsen, C., R. Siddans, S. Dean, R. Grainger, G. Thoams, and P. D. Watts (2005), Cloud Parameter Retrievals from ATSR-2, in *Proceedings of the MERIS (A)ATSR Workshop 2005 (ESA SP-597). 26–30 September 2005 ESRIN*, edited by H. Lacoste, p. 3.1, Frascati, Italy, Published on CDROM.

Press, W. H., S. A. Teukolsky, W. T. Vetterling, and B. P. Flannery (1992), *Numerical recipes in FORTRAN. The art of scientific computing*, 2nd ed., University Press, Cambridge.

Richter, A., J. P. Burrows, H. Nüß, and C. Granier (2005), Increase in tropospheric nitrogen dioxide over China observed from space, *Nature*, 437, 129–132, doi:10.1038/nature04092.

Rodgers, C. (2000), *Inverse methods for atmospheric sounding: Theory and practice*, World Sc., River Edge, N. J.

Rossow, W. B., and R. A. Schiffer (1999), Advances in understanding clouds from ISCCP., *Bull. Am. Met. Soc.*, 80, 2261–2288.

Rothman, L. S., et al. (2005), The HITRAN 2004 molecular spectroscopic database, *J. Quant. Spectrosc. Radiat. Transfer*, 96, 139–204.

Rozanov, V. V., and A. A. Kokhanovsky (2004), Semianalytical cloud retrieval algorithm as applied to the cloud top altitude and the cloud geometrical thickness determination from top-of-atmosphere reflectance measurements in the oxygen A band, *J. Geophys. Res.*, 109, D05202, doi:10.1029/2003JD004104.

Rozanov, V. V., A. A. Kokhanovsky, and J. Burrows (2004), The determination of cloud altitudes using GOME reflectance spectra: Multilayered cloud systems, *IEEE Trans. Geosci. Remote Sens.*, 42, 1009–1017.

Rozanov, V. V., A. A. Kokhanovsky, T. R. Siddans, B. Latter, A. Stevens, and J. Burrows (2006), Intercomparison of cloud top altitudes as derived using GOME and ATSR-2 instruments onboard ERS-2, *Remote Sens. Environ.*, 102, 186–193, doi:10.1016/j.rse.2006.02.009.

Schaub, D., K. F. Boersma, J. W. Kaiser, A. K. Weiss, D. Folini, H. J. Eskes, and B. Buchmann (2006), Comparison of GOME tropospheric NO_2 columns with NO_2 profiles deduced from ground-based in situ measurements, *Atmos. Chem. Phys.*, 6, 3211–3229.

Schutgens, N. A. J., and P. Stammes (2003), A novel approach to the polarization correction of spaceborne spectrometers, *J. Geophys. Res.*, 108(D7), 4229, doi:10.1029/2002JD002736.

Sherwood, S. C., J.-H. Chae, P. Minnis, and M. McGill (2004), Underestimation of deep convective cloud tops by thermal imagery, *Geophys. Res. Lett.*, 31, L11102, doi:10.1029/2004GL019699.

Stam, D. M., J. F. De Haan, J. W. Hovenier, and I. Aben (2000), Detecting radiances in the O_2 A band using polarization-sensitive satellite instruments with application to the Global Ozone Monitoring Experiment, *J. Geophys. Res.*, 105(D17), 22,379–22,392, doi:10.1029/2000JD900313.

Thompson, A. M., D. P. McNamara, K. E. Pickering, and R. D. McPeters (1993), Effect of marine stratocumulus on TOMS ozone, *J. Geophys. Res.*, 98(D12), 23051–23057, doi:10.1029/93JD01618.

Tikhonov, A. (1963), On the solution of incorrectly stated problems and a method of regularization, *Dokl. Akad. Nauk SSSR*, 151, 501–504.

Tilstra, L. G., G. van Soest, and P. Stammes (2005), Method for in-flight satellite calibration in the ultraviolet using radiative transfer calculations, with application to Scanning Imaging Absorption Spectrometer for Atmospheric Chartography (SCIAMACHY), *J. Geophys. Res.*, 110, D18311, doi:10.1029/2005JD005853.

Tran, H., C. Boulet, and J.-M. Hartmann (2006), Line mixing and collision-induced absorption by oxygen in the A band: Laboratory measurements, model, and tools for atmospheric spectra computations, *J. Geophys. Res.*, 111, D15210, doi:10.1029/2005JD006869.

Tuinder, O. N. E., R. de Winter-Sorkina, and P. J. H. Builtjes (2004), Retrieval methods of effective cloud cover for the GOME instrument: An intercomparison, *Atmos. Chem. Phys.*, 4, 255–273.

van de Hulst, H. C. (1957), *Light Scattering by small particles*, John Wiley and Sons, New York.

van Deelen, R., O. P. Hasekamp, and J. Landgraf (2007), Accurate modeling of spectral fine-structurefine-structure in Earth radiance spectra measured with the Global Ozone Monitoring Experiment, *Appl. Opt.*, *46*, 243–252.

van Diedenhoven, B., O. P. Hasekamp, and I. Aben (2005), Surface pressure retrieval from SCIAMACHY measurements in the O_2 A band: Validation of the measurements and sensitivity on aerosols, *Atmos. Chem. Phys.*, *5*, 2109–2120.

van Diedenhoven, B., O. P. Hasekamp, and J. Landgraf (2006), Efficient vector radiative transfer calculations in vertically inhomogeneous cloudy atmospheres, *Appl. Opt.*, *45*, 5993–6006.

Van Roozendael, M., et al. (2006), Ten years of GOME/ERS-2 total ozone data—the new GOME data processor (GDP) version 4: 1. Algorithm description, *J. Geophys. Res.*, *111*, D14311, doi:10.1029/2005JD006375.

Wang, J., W. B. Rossow, and Y. Zhang (2000), Cloud vertical structure and its variations from a 20-yr global Rawinsonde dataset, *J. Clim.*, *13*, 3041–3056.

Wang, P., P. Stammes, and F. Boersma (2006), Impact of the effective cloud fraction assumption on tropospheric NO_2 retrievals, in *Proceedings of the First Atmospheric Science Conference*, Frascati, Italy (ESA SP-628).

Watts, P. D., C. T. Mutlow, A. J. Baran, and A. M. Zavody (1998), Study on cloud properties derived from meteosat second generation observations, EUMETSAT ITT no. (97/181).

Yang, Z., P. O. Wennberg, R. P. Cageao, T. J. Pongetti, G. C. Toon, and S. P. Sander (2005), Ground-based photon path measurements from solar absorption spectra of the O_2 A-band, *J. Quant. Spectrosc. Radiat. Transfer*, *90*, 309–321.

———————————

O. Hasekamp, J. Landgraf, and B. van Diedenhoven, SRON Netherlands Institute for Space Research, Utrecht, The Netherlands. (b.van.diedenhoven@sron.nl)